# Extreme optical chirality of plasmonic nanohole arrays due to chiral Fano resonance

A. V. Kondratov,[1,*] M. V. Gorkunov,[1,2] A. N. Darinskii,[1] R. V. Gainutdinov,[1] O. Y. Rogov,[1] A. A. Ezhov,[1,3] and V. V. Artemov[1]

[1]*Shubnikov Institute of Crystallography of Federal Scientific Research Centre "Crystallography and Photonics"*
*of Russian Academy of Sciences, 119333 Moscow, Russia*
[2]*National Research Nuclear University MEPhI (Moscow Engineering Physics Institute), 115409 Moscow, Russia*
[3]*Faculty of Physics, Lomonosov Moscow State University, 119991 Moscow, Russia*

We study the physical origin of extreme optical chirality of subwavelength arrays of chiral holes in metal. We reconstruct the nanoscale relief of the hole arrays by the atomic-force microscopy and post-process the data to acquire an average unit-cell shape clear of noise and defects. For this shape, we perform the electromagnetic finite difference time domain simulations that reproduce all important features observed by the light-transmission experiments, including the notably strong circular dichroism and optical activity covering the whole range of possible values. To interpret the simulation results, we develop a chiral coupled-mode model which yields analytical expressions that fit accurately the numerical data in a broad wavelength range. Our conclusions undoubtedly link the extreme optical chirality to the plasmon resonances of chiral holes and the associated chiral Fano-type transmission resonance.

## I. INTRODUCTION

Chirality is a general attribute of various noncentrosymmetric materials and, importantly, most of biological objects and substances. However, it typically gives rise to rather weak optical effects, detection of which requires large amounts of transparent materials and precise techniques. Vast application prospects spanning from light circular polarizing [1] to chemical chirality sensing [2] and biosensing [3] entice intensive search for artificial materials with higher degree of optical chirality.

Chiral metamaterials, regular subwavelength arrays of elements with broken mirror symmetry, are prominent for very strong optical chirality [4]. One can divide the diverse variety of chiral metamaterials emerged over the past decade into those made of elements of truly chiral shapes and the planar ones, so-called two-dimensional (2D) chiral, that lack the in-plane mirror symmetry but are reflection symmetric with respect to the structure plane (see, e.g., Ref. [5]). For the latter, the optical chirality is forbidden by the symmetry restrictions which can be lifted by dielectric substrates: a difference between the top and bottom substrates effectively turns a 2D-chiral array into a truly chiral one [6]. However, the optical chirality of such planar structures remains low while a moderate shape modification of metal elements that breaks their mirror symmetry produces much stronger chirality enhancement [7].

Using sophisticated techniques, metamaterials consisting of various submicron size chiral elements have been fabricated. Multilayer arrays of coupled split ring resonators have shown a chiral response at the wavelengths of a few microns [8], while twisted stacks of nanorod arrays provided it in the red and near-infrared ranges [9]. For the visible, nanosize dielectric helices decorated with silver nanoparticles [10], arrays of metallic helices [11], and starfish-shaped metal elements [7] exhibited a notably strong chirality with the optical activity (OA) and circular dichroism (CD) of a few tens of degrees.

In this context, subwavelength arrays of light-transmitting chiral holes in metal are quite remarkable: their OA and CD can eventually reach extreme (maximum and minimum possible) values [12,13]. The arrays exhibit sophisticated spectra of OA an CD in the visible, which curiously transform as the metal thickness or the hole shape are varied. Complex links between the spectra of OA and CD have been established using the generalized Kramers-Kronig relations [13]. However, the origin of peculiar spectral dependencies is yet unexplained. The aim of this paper is to reveal the physical mechanism responsible for the extreme chirality of the hole arrays, which is of the key importance for the design of further ultrachiral metamaterials and optimizing their performance.

Optical properties of metal nanostructures are strongly determined by their plasmon resonances and are very sensitive to the structure shape [14,15] and its small perturbations [16,17]. Therefore, in our electromagnetic simulations we had to rely on the precise shape of chiral holes reconstructed by the atomic-force microscopy (AFM). The shape complexity and, especially, the high aspect ratio of the holes required us to develop a specific AFM technique as discussed in Sec. II. For the resolved shapes, the finite difference time domain (FDTD) simulations yielded results described in Sec. III, which reproduce nicely the main features observed by experiments. For a qualitative explanation, the general principles of symmetry and reciprocity are considered in Sec. IV A. A quantitative interpretation is given in terms of the chiral coupled-mode (CM) model which we describe in Sec. IV B with more details provided in the Appendixes. Our conclusions on the origin of extreme optical chirality of nanohole arrays are given in Sec. V.

## II. RECONSTRUCTION OF CHIRAL HOLE SHAPE

For metal objects of simple geometry, three-dimensional (3D) models suitable for the full-scale electromagnetic simulations can be combined from basic 3D shapes with appropriately rounded edges. Using also tabulated experimental values of the metal permittivity can provide a reasonable agreement of simulations and experiment (see, e.g., the recent Ref. [18]).
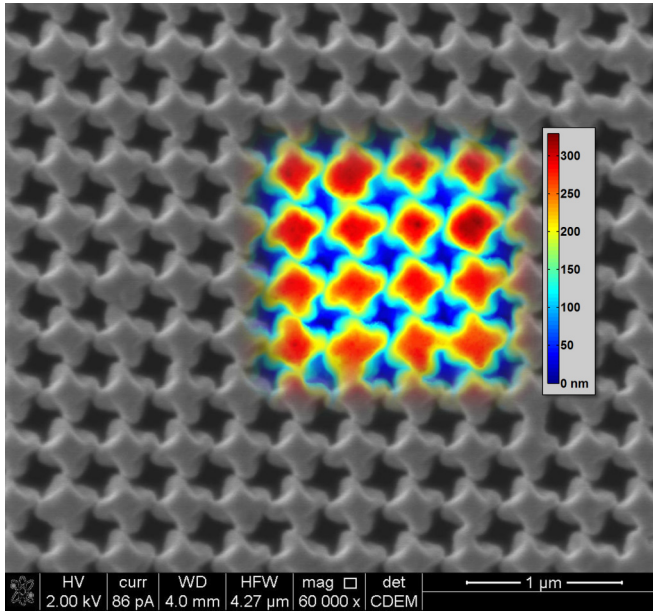
---

*kondratov@crys.ras.ru

FIG. 1. SEM image of the chiral hole array milled in a 270-nm-thick freely suspended silver foil that exhibited extreme optical chirality [12] and an AFM image of a fragment of its analog made on a glass substrate (shown as a color map inset).



FIG. 2. A unit cell of the chiral hole array as resolved by AFM (a) and its final 3D model (b) created from the processed AFM data (the inset).

In this work, however, we are interested in fine polarization features of light transmitted by the arrays of chiral holes which have a rather complex and not initially fully known shape. The reported arrays [12] were milled in freely suspended silver films by a focused ion beam (FIB) controlled by digital templates. The latter determined the hole shape as a 4-start screw thread circular hole, but it was clear that the hole final shape was different from the template due to the inevitable ion beam defocusing and partial diversion (see also Fig. 1).

At present, AFM is the most advanced approach for precise reconstruction of surface reliefs with a nanometer resolution. By default, the technique is best suited for reconstructing the reliefs with low height-to-width ratio, when a most common vertical AFM probe can subsequently scan over the lateral dimensions with the probe tip always kept at a close distance to the surface. In our case, the chiral holes have the inner diameter below 200 nm (according to the SEM data) and are milled in silver films of the thickness of 270 nm and more. The common AFM probes with large apex angles are not suitable here as they produce blind areas over considerable parts of the holes. Therefore, for reconstructing the hole array shape, ordinary silicon AFM probes were customized by FIB sharpening which yielded the probes of a few microns height, with an apex angle about $10°$ and a tip curvature radius of 10 nm. Such tip parameters were sufficient for reconstructing the fine elements of the chiral hole shape.

The arrays studied in Ref. [12] were milled in freely suspended silver foils which are not mechanically stable for AFM measurements. Therefore, we have performed the measurements on similar hole arrays milled in silver films on glass substrates using the same FIB digital templates.

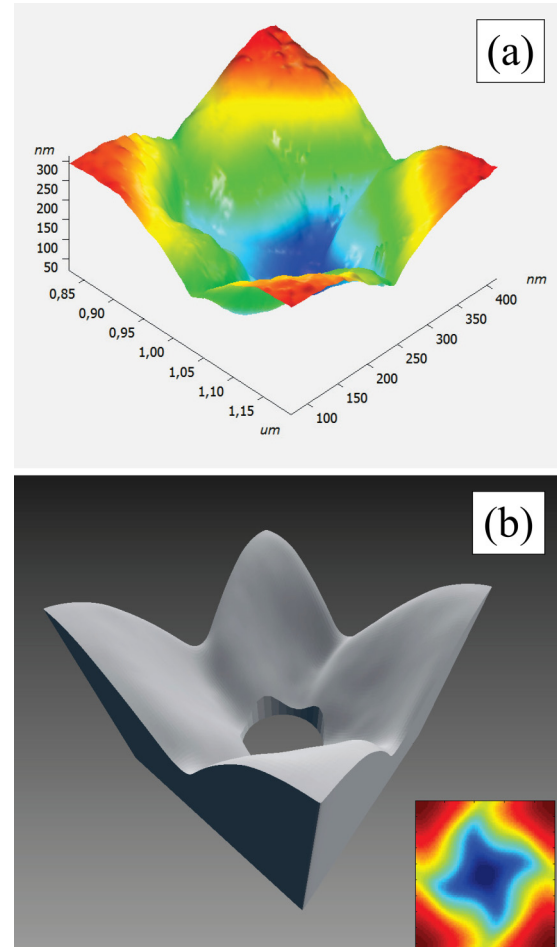The acquired raw AFM data (see the inset in Fig. 1 for an example) can be slightly misoriented and include systematic errors due to the finite tip size as well as a noticeable random noise arising from the structure roughness and defects [see also Fig. 2(a)]. In order to resolve the average structure unit cell, we developed a numeric routine that minimizes the systematic and stochastic errors keeping intact the distinctive periodic features.

First, to compensate for the finite AFM tip curvature radius (which makes the holes narrower and more shallow), the effective tip radius of 10 nm was subtracted from the AFM data along the direction normal to the metal surface. Notably, this primary post-processing adjusted the hole size and depth to the values much closer to those seen in the scanning electron microscopy (SEM) images.

Next, to reduce the effects of the random noise and defects, a two-step averaging over the unit cells of the structure was performed: on the first step, an average hole shape with equal contribution of all the structure units was computed; on the second step, higher outliers with respect to this average were neglected.

To ensure the precise fourfold symmetry, the unit cell was averaged with its images rotated by $90°$, $180°$, and $270°$. Finally, the spatial periodicity inherent to the hole array was to be ensured. As we did not account for it so far,

deviations from the exact periodicity were used as an estimate of the overall shape reconstruction error and we found that it did not to exceed a few nanometers. To provide the exact periodicity, the mismatch of the metal relief at the opposite unit-cell boundaries was compensated by a slight deformation of the adjacent metal surface. The resulting 3D model of the chiral hole is strictly periodic, fourfold symmetric, and much smoother than its representative analog taken directly from the AFM data [compare Figs. 2(a) and 2(b)].

## III. SIMULATIONS

Precise full-scale numerics of the optics of plasmonic nanostructures remains challenging even with the use of high-performance workstations. In particular, FDTD technique requires extremely fine space partitioning with the grid step about a nanometer and less to achieve a reasonable convergence [19].

Simulations of the light transmission through chiral hole arrays were performed on a workstation equipped with a pair of 10-core Intel Xeon CPUs and an Nvidia Tesla K40 GPGPU using commercial SPEAG SEMCAD X FDTD solver accelerated by Acceleware CUDA library. The latter significantly reduced the running time which allowed us to use a single workstation instead of a computing cluster. A reasonable balance between the simulation time and convergence was achieved with the 1-nm FDTD mesh step.

In our modeling, the metal was characterized by a homogeneous, isotropic, and local permittivity. Note that these three assumptions can be fairly approximate in the optics of nanoscale silver structures and even under them there remains a freedom of choosing appropriate values of the silver permittivity which are different for monocrystalline and polycrystalline samples, depend on the temperature [20] and the surface quality [21]. However, our main interest here is the origin of extremely chiral light transmission, and we chose for simplicity the silver permittivity within the three-pole generic

dispersive model [22]:

$$\tilde{\varepsilon}(\omega) = \varepsilon_\infty + i\frac{\sigma}{\varepsilon_0\omega} + \sum_{p=1}^{3}\frac{A_p}{B_p\omega^2 - iC_p\omega + D_p}, \quad (1)$$

with the values of $\varepsilon_\infty$, $\sigma$, $A_p$, $B_p$, $C_p$, and $D_p$ adjusted to fit the experimental reference data [23].

A comparison of the transmission characteristics observed in Ref. [12] for a 270-nm-thick array with those obtained numerically is presented in Fig. 3. As shown in Figs. 3(a) and 3(b), the calculated spectrum of transmission of linearly polarized light reproduces the main features seen in the experiments: there is a pronounced transmission band at larger wavelengths and a peculiar weaker maximum close to the short-wavelength border of the visible range. In-between, the simulated transmittance falls below the 1% level similarly to the experimental one, although the latter stays higher, most probably, due to a light leakage through defects.

We express conventionally the main characteristics of the optical chirality, CD and OA, by the the left circular polarized (LCP) and right circular polarized (RCP) transmission amplitudes $t_L$ and $t_R$ as

$$\mathrm{CD} = \frac{|t_R|^2 - |t_L|^2}{|t_R|^2 + |t_L|^2}, \quad (2)$$

$$\mathrm{OA} = \tfrac{1}{2}(\arg t_L - \arg t_R). \quad (3)$$

Note that the sign of the latter is defined as in the transmission experiment setup [12], where positive OA corresponded to the clockwise polarization rotation as seen against the transmitted-light propagation direction. The numerically obtained spectra of OA and CD shown in Fig. 3(d) clearly exhibit the same features as the experimental ones reported in Ref. [12] and shown in Fig. 3(c): CD has a pronounced single peak which is accompanied by an antiresonance of OA at the same wavelength. Note that in both cases, OA covers all its possible values in the adjacent wavelength
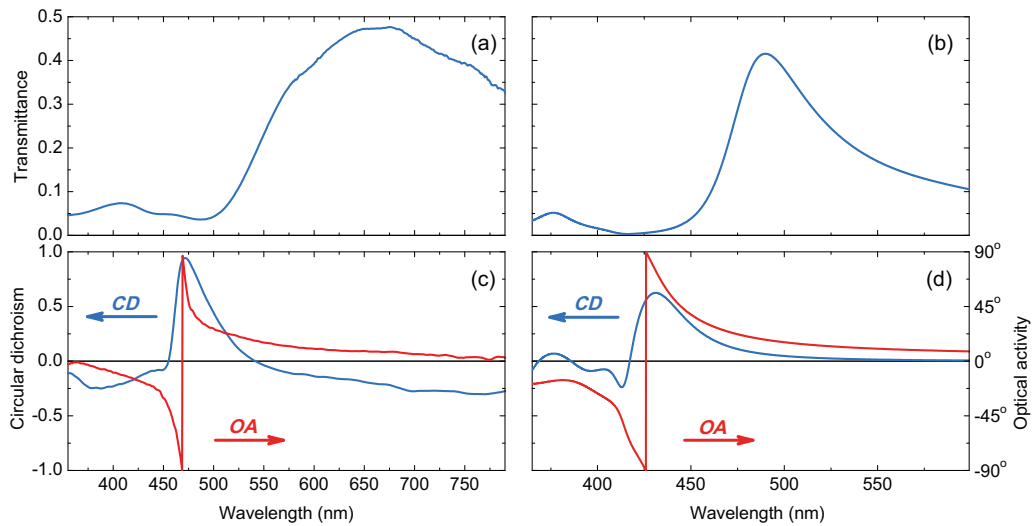


FIG. 3. Comparison of the optical properties of an array of chiral holes reported in Ref. [12] with those obtained by FDTD simulations: experimental (a) and numerical (b) transmittances of linearly polarized light; optical chirality parameters observed (c) and obtained numerically (d).

range. The calculated maximum CD values are lower than in the experiment. The nonzero long-wavelength tail of the experimental CD indicates, however, the presence of certain birefringence and linear dichroism due to the fabrication imperfections, which explains the quantitative differences.

The calculated positions of the sharp spectral features of the observables are systematically blue-shifted with respect to the experiment. Thus, the experimental transmission band starts above the wavelength of 500 nm, while the numerical transmittance goes up above 450 nm. Similarly, the numerical short-wavelength transmission peak as well as the peak of CD and antiresonance of OA are equally blue-shifted by approximately 50 nm compared to the experiment. This mismatch can be partially attributed to a slight difference between the 375-nm period of the freely suspended arrays used in the optical experiment and the 360-nm period of the array on glass substrate used for the AFM shape reconstruction. On the other hand, one might attempt also to decrease the mismatch by adjusting the silver permittivity dispersion.

We have performed the simulations for the plane waves incident on the both sides of the structure (milled and flat). The corresponding spectra of light absorption are very different as shown in Fig. 4. In the first case [Fig. 4(a)], the absorption has a well-defined resonance near the wavelength of 480 nm with a chiral split, i.e., a difference for LCP and RCP incident light. Also, there is a nonchiral resonance near the 415-nm wavelength. The flat side incidence absorption [Fig. 4(b)] has one chiral resonance at the same wavelength of 480 nm, and a weaker one near the 373-nm wavelength which possesses also a tiny chiral split. Notice the absence of the nonchiral resonance at the 415-nm wavelength here.
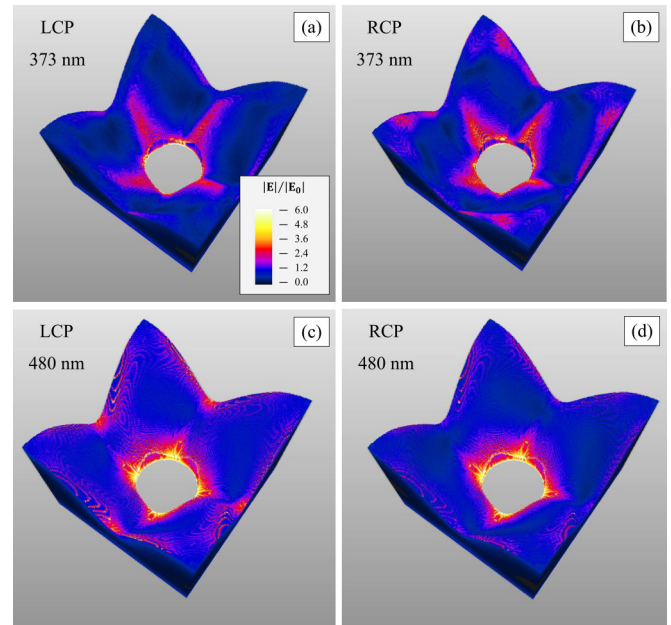


FIG. 5. Spatial structure of plasmon resonances at the wavelengths of 373 nm (a), (b) and 480 nm (c), (d) excited by LCP (a), (c) and RCP (b), (d) waves incident from the flat side of the hole array. The root mean square of the absolute surface values of electric field in metal normalized by the incident wave amplitude is shown.

Clearly, the peculiar spectral behavior of the absorption is determined by the resonances of the metal hole arrays, i.e., their plasmon resonances. The modeling revealed the general feature of the resonances: their positions and widths are independent of the handedness of the incident circularly polarized light. The latter affects only the height of the absorption peaks, i.e., the strength of the resonance excitation.

It can be seen in Fig. 5 that the spatial structure of the plasmon resonances possess certain distinct features. For the 373-nm resonance, there is a strong field localization at the narrow hole entrance, while for the one at the 480-nm wavelength, the field is spread over the metal hollows inside the hole. For both resonances, the field enhancement by a factor of up to 6 takes place.

The calculated spectra of the LCP and RCP transmission characteristics are shown in Fig. 6. We have found that in spite of the substantial difference of the absorption spectra for the different sides of incidence, the transmission amplitudes are the same within one percent accuracy. As their precise equality follows from the Lorentz lemma (see more details below in Sec. IV A and Appendix A), this is a good measure of the overall numeric error, which we thus estimate to be less than one percent.

Since CD and OA do not depend on the side of incidence, we focus in the following on the case of flat side of incidence, when the absorption has two well-defined Lorentzian peaks. The LCP and RCP transmittances shown in Fig. 6(a) exhibit a weak chiral splitting being not substantially different otherwise. Their peaks are slightly red-shifted with respect to the absorption peaks, which is characteristic for Fano-type transmission resonances. At the same time, the LCP and
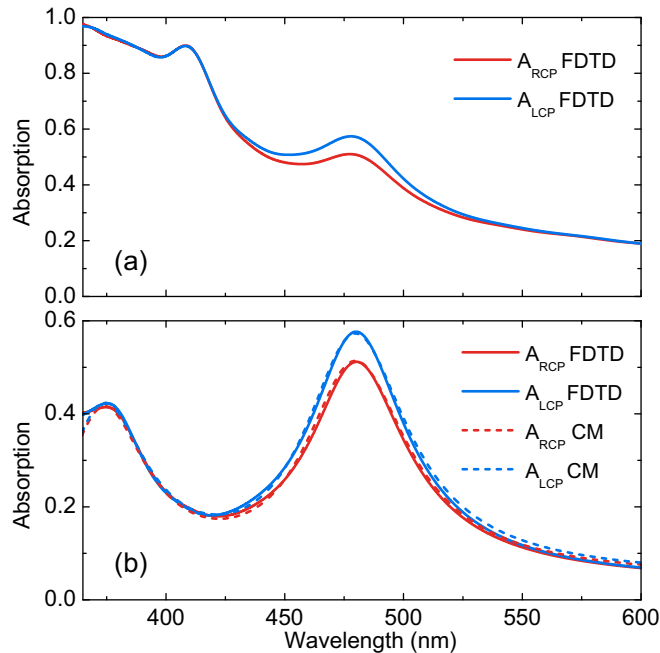


FIG. 4. Absorption spectra of LCP and RCP light incident from the milled (a) and flat (b) sides of the chiral hole array. Solid lines represent the results of numeric FDTD simulations while the dashed lines are their analytical fits by a pair of Lorentz poles as described by Eq. (18).
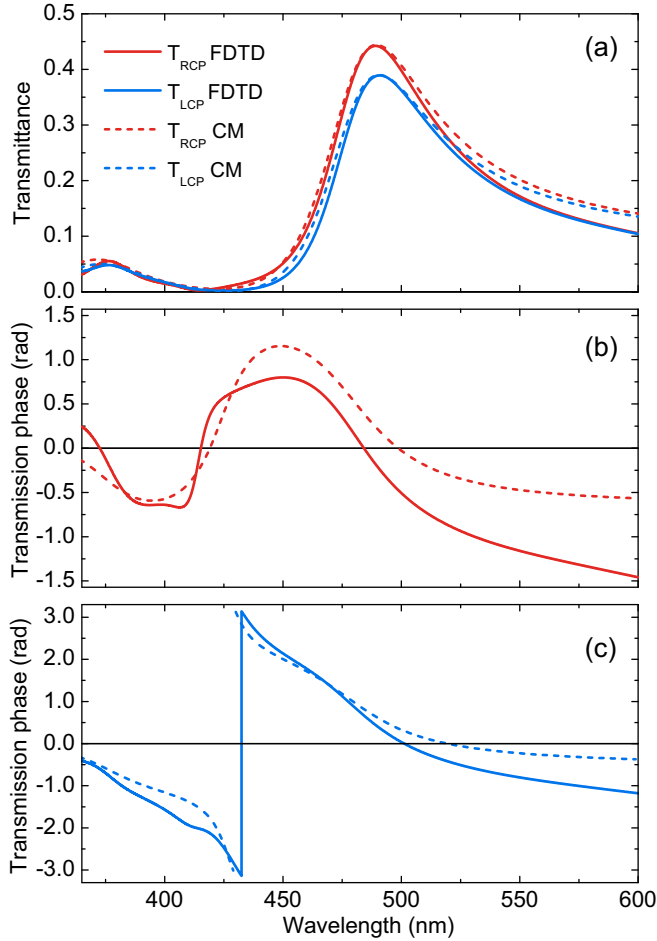
FIG. 6. Transmission characteristics for the LCP and RCP incident waves: (a) the LCP and RCP transmittances; (b), (c) the transmission phases for the LCP and RCP waves, respectively. The results of the full-scale FDTD simulations are shown by the solid lines while the dashed lines correspond to the analytical fit in accordance with the CM model (19).

RCP transmission phase spectra are qualitatively different [see Figs. 6(b) and 6(c)].

The total light energy conservation is ensured by the difference in reflection spectra for the different sides of incidence. Our general observation is the absence of chiral split of the reflectance, whichever side of incidence is considered. As discussed in Sec. IV A, the absence of chiral effects in reflection is a general attribute of structures with rotational symmetry and follows directly from the symmetry and reciprocity arguments.

## IV. THEORY

### A. Symmetry and reciprocity implications

The general features of light transmission and reflection by the fourfold rotationally symmetric arrays of chiral holes can be explained from the fundamental principles of symmetry and reciprocity. This can be conveniently done by considering the $S$-matrix formulation of the transmission-reflection problem. For clarity, one can start with the $S$-matrix problem in the basis of linear polarizations. Then, for the incident and reflected transversal waves propagating along the $z$ axis, the $S$-matrix problem reads as

$$\begin{pmatrix} b_x \\ b'_x \\ b_y \\ b'_y \end{pmatrix} = \begin{pmatrix} S_{11} & S_{12} & S_{13} & S_{14} \\ S_{12} & S_{22} & S_{23} & S_{24} \\ S_{13} & S_{23} & S_{33} & S_{34} \\ S_{14} & S_{24} & S_{34} & S_{44} \end{pmatrix} \begin{pmatrix} a_x \\ a'_x \\ a_y \\ a'_y \end{pmatrix}, \quad (4)$$

where $a_i$ and $a'_i$ are the components of the amplitudes of light waves incident on different sides of the structure, and $b_i$ and $b'_i$ are those of the waves outgoing from different sides. Note that the $S$ matrix is symmetric as required by the Lorentz reciprocity lemma.

If the light is incident normally on the planar array with a fourfold rotational symmetry, the $S$ matrix in Eq. (4) must be invariant under $\pm\pi/2$ rotations about the $z$ axis. This implies equalities $S_{33} = S_{11}$, $S_{44} = S_{22}$, $S_{34} = S_{12}$, $S_{23} = -S_{14}$, $S_{13} = -S_{13} = 0$, and $S_{24} = -S_{24} = 0$, which reduce the $S$ matrix to the form

$$\hat{S}^{(xy)} = \begin{pmatrix} S_{11} & S_{12} & 0 & S_{14} \\ S_{12} & S_{22} & -S_{14} & 0 \\ 0 & -S_{14} & S_{11} & S_{12} \\ S_{14} & 0 & S_{12} & S_{22} \end{pmatrix}. \quad (5)$$

For the chiral arrays, it is convenient to use the basis of waves of circular polarizations of definite handedness, i.e., with the electric field rotating clockwise or anticlockwise when seen against the $z$-axis direction. The corresponding complex unit vectors are

$$\mathbf{e}_{\pm} = \frac{1}{\sqrt{2}}(\mathbf{e}_x \mp i\mathbf{e}_y). \quad (6)$$

In this basis, the "+" waves are RCP when they propagate along the $z$ axis and LCP when they propagate against it. For the "−" waves, the opposite is true.

The $S$ matrix in this basis can be obtained as $\hat{S} = \hat{T}_c \hat{S}^{(xy)} \hat{T}_c^+$, where

$$\hat{T}_c = \frac{1}{\sqrt{2}} \begin{pmatrix} 1 & 0 & -i & 0 \\ 0 & 1 & 0 & -i \\ 1 & 0 & i & 0 \\ 0 & 1 & 0 & i \end{pmatrix}, \quad (7)$$

and then

$$\hat{S} = \begin{pmatrix} S_{11} & S_{12} + iS_{14} & 0 & 0 \\ S_{12} - iS_{14} & S_{22} & 0 & 0 \\ 0 & 0 & S_{11} & S_{12} - iS_{14} \\ 0 & 0 & S_{12} + iS_{14} & S_{22} \end{pmatrix}. \quad (8)$$

The physical meaning of the elements of this matrix can be easily identified by writing the corresponding analog of Eq. (4) in the basis (6):

$$\begin{pmatrix} b_+ \\ b'_+ \\ b_- \\ b'_- \end{pmatrix} = \begin{pmatrix} r & t_L & 0 & 0 \\ t_R & r' & 0 & 0 \\ 0 & 0 & r & t_R \\ 0 & 0 & t_L & r' \end{pmatrix} \begin{pmatrix} a_+ \\ a'_+ \\ a_- \\ a'_- \end{pmatrix}, \quad (9)$$

where the transmission amplitudes of the left and right circularly polarized light, $t_L$ and $t_R$, together with the reflection amplitudes from different sides of the structure, $r$ and $r'$, have
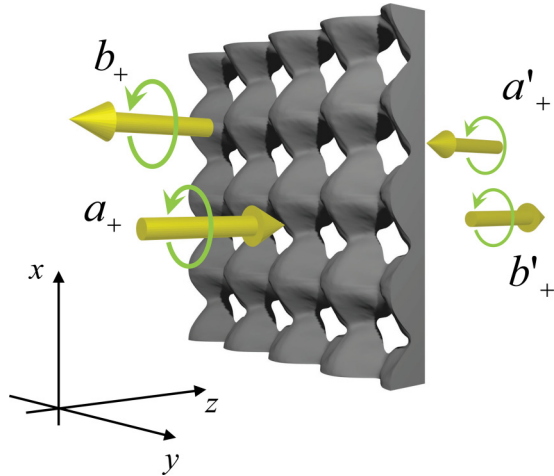
FIG. 7. Sketch of one of the enclosed transmission-reflection problems for an array of the fourfold rotational symmetry.

been introduced, and the symmetry of the matrix (8) has been taken into account.

The block-diagonal form of the $S$ matrix in Eq. (9) implies the independence of the two enclosed transmission-reflection problems relating the waves with the same handedness: the incident $a_+$ and $a'_+$ with the outgoing $b_+$ and $b'_+$; and the incident $a_-$ and $a'_-$ with the outgoing $b_-$ and $b'_-$. The first problem is illustrated in Fig. 7, which shows also why the same handedness (the same direction of field rotation) is assigned to the counterpropagating beams with the opposite circular polarizations. Note that the $S$ matrix in Eq. (9) is not simply symmetric but also requires a simultaneous "+" $\leftrightarrow$ "−" (or, equivalently, $L \leftrightarrow R$) interchange, which reflects the peculiarities of the Lorenz reciprocity lemma application to circularly polarized waves (see Appendix A).

The $S$-matrix equation (9) alone puts substantial restrictions on the properties of chiral structures of the fourfold rotational symmetry: (i) the transmission amplitudes of the waves of the opposite handedness incident on different sides (i.e., of the same circular polarization) are equal; (ii) the reflection amplitudes are independent of the wave handedness, i.e., the reflections are achiral.

It can be also readily shown that the transmission chirality strongly depends on the dissipative losses in the structure. Indeed, in the absence of losses, the system is reversible and its $S$ matrix is unitary, $\hat{S}^+\hat{S} = 1$. This requires $|t_R|^2 = |t_L|^2 = 1 - |r|^2 = 1 - |r'|^2$, which means, in particular, the absence of CD. OA, however, can still be present due to possibly different phases of $t_R$ and $t_L$.

## B. Chiral coupled-mode model

To clarify the physics responsible for the rather peculiar spectral behavior of optical observables, we develop an analytical model that accounts for the plasmon resonances and their contribution to the chiral light transmission: a chiral CM model. Having much in common with simpler CM models that have been used to understand the light transmission through arrays of nonchiral holes and slits in dielectric and metal films [24–26], such a model here should take into

account the structure chirality as well as the presence of two plasmon resonances at different wavelengths. Typically, a good quantitative agreement can be achieved by using a simple CM model only in a narrow frequency range close to a single resonance. Here, we have to cover a broader range that includes both resonances of the array. As shown below, this allows reproducing the main observable features although the accuracy is somewhat lower than of the CM modeling of plasmonic systems in a much narrower wavelength range [26].

In a CM model, without going into microscopic details, one can describe the dynamics of plasmon resonances by their slow varying amplitudes. The above numerics has revealed that the hole arrays support plasmon resonances at two well-separated resonant wavelengths. At each wavelength, a plasmon of certain handedness can be excited by the electromagnetic waves of the same handedness. While the positions and widths of the resonances are independent of the handedness, the strength of the plasmon excitation moderately depends on it.

Accordingly, we introduce the plasmon amplitudes

$$\mathbf{p}_\nu = \begin{pmatrix} p_{\nu+} \\ p_{\nu-} \end{pmatrix}, \tag{10}$$

where the index $\nu = 1,2$ enumerates the plasmons with different resonant wavelengths. For each wavelength, a conjugate pair of plasmons with the amplitudes $p_{\nu-}$ and $p_{\nu+}$ can be excited. The $\pm$ signs denote the plasmon handedness that coincides with that of the circular polarization eigenvectors (6).

Then, the plasmon excitation by the incoming plane waves can be described by the equation

$$\frac{d\mathbf{p}_\nu}{dt} = \sum_{\nu'=1,2} \hat{\mathbf{Q}}_{\nu\nu'}\mathbf{p}_{\nu'} + \hat{\mathbf{M}}_\nu\mathbf{a}, \tag{11}$$

while the irradiation of the outgoing waves is governed by the relation

$$\mathbf{b} = \sum_{\nu=1,2} \hat{\mathbf{N}}_\nu\mathbf{p}_\nu + \hat{\mathbf{C}}\mathbf{a}. \tag{12}$$

Here, as in Eq. (9), the incoming and outgoing wave amplitudes are given by the vectors $\mathbf{a}$ and $\mathbf{b}$, respectively.

The matrix $\hat{\mathbf{Q}}_{\nu\nu'}$ determines the spectrum of plasmon resonances and an internal energy exchange between them. The matrix of the direct transmission reflection is supposed to have a simple nonchiral form

$$\hat{\mathbf{C}} = \begin{pmatrix} \rho & \tau & 0 & 0 \\ \tau & \rho' & 0 & 0 \\ 0 & 0 & \rho & \tau \\ 0 & 0 & \tau & \rho' \end{pmatrix}. \tag{13}$$

The matrix of coupling constants between the $\nu$-th plasmon and the incoming waves is taken as

$$\hat{\mathbf{M}}_\nu = \begin{pmatrix} m_{\nu+} & m'_{\nu+} & 0 & 0 \\ 0 & 0 & m_{\nu-} & m'_{\nu-} \end{pmatrix}, \tag{14}$$

and the matrix of coupling constants between the outgoing waves and the $\nu$-th plasmon reads as

$$\hat{\mathbf{N}}_\nu = \begin{pmatrix} n_{\nu+} & 0 \\ n'_{\nu+} & 0 \\ 0 & n_{\nu-} \\ 0 & n'_{\nu-} \end{pmatrix}. \tag{15}$$

To ensure the Lorentz reciprocity (see Appendix A), the coupling matrices $\hat{\mathbf{N}}_\nu$ are to be equal to $\hat{\mathbf{M}}_\nu$ transposed and subjected to the "+" $\leftrightarrow$ "−" interchange, i.e., $n_{\nu\pm} = m_{\nu\mp}$ and $n'_{\nu\pm} = m'_{\nu\mp}$.

Since in our case the plasmons with different $\nu$ are well separated, we can neglect their internal interaction. The energy exchange between the plasmons $p_{\nu-}$ and $p_{\nu+}$ of different handedness is forbidden by the symmetry. Therefore, we write

$$\hat{\mathbf{Q}}_{\nu\nu'} = \delta_{\nu\nu'} \begin{pmatrix} q^{(\nu)} & 0 \\ 0 & q^{(\nu)} \end{pmatrix} \qquad (16)$$

with $q^{(\nu)} = i(\omega - \omega^{(\nu)}) - \gamma^{(\nu)}$, where $\omega^{(\nu)}$ and $\gamma^{(\nu)}$ are the plasmon resonant frequencies and damping constants, respectively.

For a steady state with $d\mathbf{p}_\nu/dt = 0$, one immediately obtains from Eqs. (11) and (12) the particular form of Eq. (9) with

$$\hat{\mathbf{S}} = \hat{\mathbf{C}} - \sum_{\nu=1,2} \frac{1}{q^{(\nu)}} \hat{\mathbf{N}}_\nu \hat{\mathbf{M}}_\nu. \qquad (17)$$

If one assumes that the energy dissipation and the related nonreversibility of the system are determined solely by the nonradiant plasmon damping, the direct transmission-reflection matrix $\hat{\mathbf{C}}$ and the coupling matrices $\hat{\mathbf{N}}_\nu$ and $\hat{\mathbf{M}}_\nu$ are the same as in a similar lossless system with zero light absorption. As shown in Appendix B, this puts remarkable general restrictions on them.

Introducing the plasmon-driven light energy dissipation in metal, one can derive physically transparent relations for the light absorption rates and transmission amplitudes (see Appendix C). In particular, the frequency dependencies of the absorption rates of the LCP and RCP light have a simple analytical form

$$A = \frac{A_1 \gamma^{(1)2}}{(\omega^{(1)} - \omega)^2 + \gamma^{(1)2}} + \frac{A_2 \gamma^{(2)2}}{(\omega^{(2)} - \omega)^2 + \gamma^{(2)2}}. \qquad (18)$$

The corresponding transmission amplitudes depend on the frequency as

$$t_{R,L} = \tau + \frac{\gamma^{(1)} t_{1R,L}}{i(\omega^{(1)} - \omega) + \gamma^{(1)}} + \frac{\gamma^{(2)} t_{2R,L}}{i(\omega^{(2)} - \omega) + \gamma^{(2)}}, \qquad (19)$$

i.e., exhibit a frequency dispersion characteristic for Fano-type transmission resonances similarly to the simpler cases studied, e.g., in Refs. [25,26].

Relations (18) and (19) have been used subsequently to fit the numerical data. First, fitting the absorption spectra [see Fig. 4(b)] yielded the plasmon resonant frequencies $\omega^{(1)}$, $\omega^{(2)}$ corresponding to the wavelengths of 373 and 480 nm. The resonance half-widths ($\gamma^{(1)}$ and $\gamma^{(2)}$) were found to be 21.9 and 26.5 nm on the wavelength scale, respectively. Next, these main resonance parameters were fixed and fitting the transmittance spectra [Fig. 6(a)] was performed in order to determine the remaining model parameters: the background nonresonant transmission amplitude $\tau = 0.210$, and the resonant transmission amplitudes $t_{1R} = 0.140 \exp(0.220i)$, $t_{1L} = 0.136 \exp(0.266i)$, $t_{2R} = 0.655 \exp(1.93i)$, $t_{2L} = 0.600 \exp(1.50i)$. Note that although only the absolute values of the transmission amplitudes were fitted, the transmission phases evaluated for the resolved
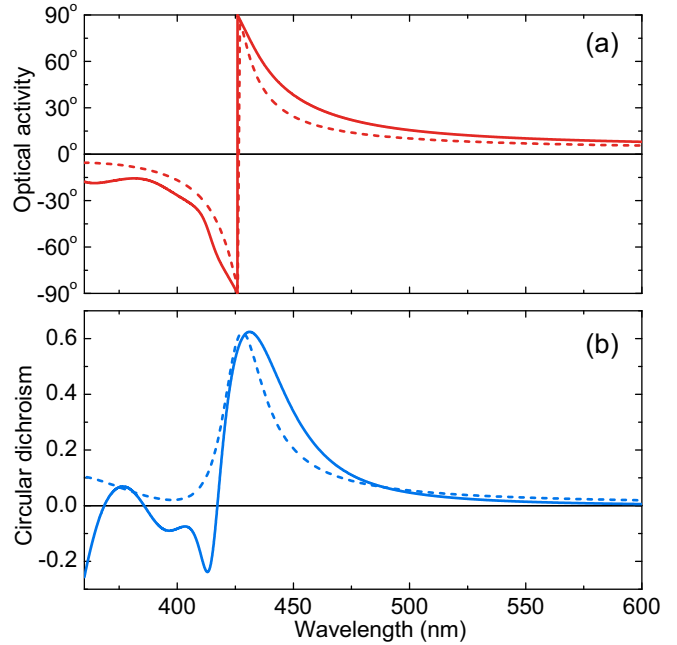


FIG. 8. Optical activity (a) and circular dichroism (b) spectra obtained by the FDTD simulations (solid line) and their analytical fit using the CM model (19) (dashed line).

model parameters were also in a good quantitative agreement with the numerical results [see Figs. 6(b) and 6(c)]. Being not surprising in the view of the Kramers-Kronig relations imposed on the complex transmission amplitudes, this indicates the self-consistence of our approach. The corresponding spectra of CD and OA evaluated analytically (see the dashed lines in Fig. 8) nicely reproduced the main features of the numerical results with a good quantitative accuracy: CD peak and the accompanying OA discontinuity occur at practically the same wavelength and they reach the same values.

## V. DISCUSSION

Performing thorough full-scale numerical electromagnetic simulations for the precisely reconstructed shape of chiral metal hole arrays allowed us to reproduce the main features of the extremely chiral light transmission reported in Ref. [12]. On the other hand, we have seen that all the complex spectral dependencies obtained numerically can be adequately explained in terms of a CM model based on a few clear assumptions and including a small number of fitting parameters with a transparent physical meaning. The CM analytics coincides with the first-principle numeric data in a wide wavelength range from 370 to 600 nm, which indicates that it is not just a convenient fitting tool but reflects the physics underlying the extreme chirality.

According to the CM model, the substantial chirality of the hole shape gives rise to a still rather moderate chiral split of the plasmon properties (the strengths of the coupling of plasmons to the incoming and outgoing plane waves). This split does not provide a notable chirality to the optical transmission, if it had not been for an interference of the chiral resonant transmission channel with a weak achiral

background transmission channel. The interference creates a chiral Fano-type transmission resonance with a pronounced split of the dips of the LCP and RCP transmittances. This gives rise to a pronounced peak of CD which is accompanied by a fast variation of OA that takes all its possible values within the adjacent wavelength range.

This mechanism explains, in particular, why the chiral hole arrays exhibit a stronger optical chirality compared to arrays of various chiral metal particles extensively studied in the recent years [7–11]. According to our conclusions, the emergence of extreme chirality requires a weak background transmission channel. This channel is weak indeed in arrays of subwavelength holes in metal and is considerably higher in arrays of metal particles on transparent substrates.

Therefore, one can expect a similarly strong optical chirality from various holey chiral nanostructures and also, more generally, from other types of structures with a chiral transmission accompanied by a weak background transmission leading to a chiral Fano-type transmission resonance. Recent calculations of the strongly chiral light transmission and diffraction by planar arrays of 2D-chiral holes in a metal film placed between different dielectric substrates [27] provide an interesting evidence of this.

Analyzing optical properties of the chiral hole arrays allowed us to formulate also a few more general rules based solely on the principles of symmetry and reciprocity and applicable to a very broad range of chiral metamaterials. The following statements are valid actually for an arbitrary chiral rotationally symmetric metamaterial upon normal electromagnetic wave incidence:

(i) Polarization conversion during reflection is absent and, accordingly, the reflections are totally achiral.

(ii) The chiral selectivity of the transmission is directly related to the chiral selectivity of the energy dissipation and no CD is possible in lossless materials.

(iii) There are no basic restrictions imposed on OA.

Historically, theoretical analysis of such chiral metamaterials has been focused mainly on their transmission characteristics (see, for example, Refs. [28,29]) and not much attention has been paid to the simple fact (i) that concerns the reflections. However, it follows directly from the Lorentz reciprocity (see Sec. IV A) and being combined with the energy conservation law leads directly to the statement (ii). The latter has been already proven independently by analyzing the transmission of lossless structures [28] or by considering their *S*-matrix properties [12].

The conclusion (ii) apparently narrows the potential range of functional properties of rotationally symmetric metamaterials, as they can possibly operate as circular polarizers only similarly to conventional dichroic linear polarizers, which transmit one polarization and dissipate the other. A possibility to overcome this can be sought in light diffracting and scattering structures. Our general conclusions do not imply the particular nature of energy dissipation, which can occur due to scattering, thus preserving a part of the light energy in the form of electromagnetic radiation. Note that Fano-type resonances can occur in such case as well [30].

Finally, the statement (iii) ensures that it is possible to design an almost lossless material that will rotate all incoming linear polarizations by the same arbitrarily large

angle. Although an example of such structure operating in the microwave range has been reported [31], fabricating a similar material for the visible is still challenging.

## VI. CONCLUSION

We have shown that the extreme optical activity and circular dichroism of light-transmitting arrays of chiral holes in metal originate from a chiral Fano-type transmission resonance. The resonance occurs due to an interference of the two transmission channels: a weak achiral background transmission and a resonant chiral transmission determined by plasmons. The results concretize general rules following from the reciprocity and symmetry arguments, and clarify the directions for the search of artificial materials with strongly chiral optical response.

## APPENDIX A: LORENTZ RECIPROCITY FOR CIRCULAR POLARIZATIONS

The implications of the Lorentz lemma for circularly polarized light follow from its main integral statement

$$\int dV \mathbf{J}_1 \cdot \mathbf{E}_2 = \int dV \mathbf{J}_2 \cdot \mathbf{E}_1, \tag{A1}$$

where $\mathbf{J}_{1,2}$ are arbitrary current distributions that produce the electric fields $\mathbf{E}_{1,2}$, respectively. The main point for the circular polarizations here is that the products of vectors in Eq. (A1) are not true scalar products which imply also a complex conjugation. Indeed, the unit vectors of the circular polarizations (6) form an orthonormal basis as $\mathbf{e}_\pm \cdot \mathbf{e}_\pm^* = 1$ and $\mathbf{e}_\pm \cdot \mathbf{e}_\mp^* = 0$. However, the opposite results occur for the product that appears in Eq. (A1): $\mathbf{e}_\pm \cdot \mathbf{e}_\pm = 0$ and $\mathbf{e}_\pm \cdot \mathbf{e}_\mp = 1$.

Therefore, the Lorentz reciprocity principle applied to currents and fields with circular polarizations relates those with different handedness: $\mathbf{J}_1, \mathbf{E}_1 \propto \mathbf{e}_+$ and $\mathbf{J}_2, \mathbf{E}_2 \propto \mathbf{e}_-$ or vice versa. This, in particular, results in the nonsymmetric form of the *S* matrices and coupling matrices in Secs. IV A and IV B.

## APPENDIX B: REVERSIBILITY OF COUPLED-MODE MODEL WITHOUT DISSIPATION

Consider a time-reversible lossless system described by the CM Eqs. (11) and (12) when the light absorption in metal is absent. Time reversibility of the direct transmission-reflection process means that its matrix is unitary: $\hat{\mathbf{C}}^+ = \hat{\mathbf{C}}^{-1}$. Note that the matrix is also symmetric, which makes its Hermitian transpose equal to its complex conjugate: $\hat{\mathbf{C}}^+ = \hat{\mathbf{C}}^*$.

If the amplitudes $\mathbf{a}$, $\mathbf{b}$, and $\mathbf{p}_\nu$ satisfy the coupled-mode equations (11) and (12), so should their time-reversed coun-

terparts do. The latter can be expressed as

$$\tilde{\mathbf{a}} = \hat{\mathbf{T}}\mathbf{b}^*, \quad \tilde{\mathbf{b}} = \hat{\mathbf{T}}\mathbf{a}^*, \quad \tilde{\mathbf{p}}_\nu = \hat{\mathbf{T}}_p\mathbf{p}_\nu^*, \quad \text{(B1)}$$

where the matrices $\hat{\mathbf{T}}$ and $\hat{\mathbf{T}}_p$ produce the "+" ↔ "−" interchange:

$$\hat{\mathbf{T}} = \begin{pmatrix} 0 & 0 & 1 & 0 \\ 0 & 0 & 0 & 1 \\ 1 & 0 & 0 & 0 \\ 0 & 1 & 0 & 0 \end{pmatrix}, \quad \hat{\mathbf{T}}_p = \begin{pmatrix} 0 & 1 \\ 1 & 0 \end{pmatrix}. \quad \text{(B2)}$$

Note that $\hat{\mathbf{T}}_p^2 = \hat{\mathbf{I}}, \hat{\mathbf{T}}^2 = \hat{\mathbf{I}}$.

Substituting the amplitudes (B1) into Eq. (12) and multiplying both sides by the matrix $\hat{\mathbf{T}}$ yields

$$\mathbf{a}^* = \sum_\nu \hat{\mathbf{T}}\hat{\mathbf{N}}_\nu\hat{\mathbf{T}}_p\mathbf{p}_\nu^* + \hat{\mathbf{T}}\hat{\mathbf{C}}\hat{\mathbf{T}}\mathbf{b}^*. \quad \text{(B3)}$$

For the matrix given by Eq. (13), $\hat{\mathbf{T}}\hat{\mathbf{C}}\hat{\mathbf{T}} = \hat{\mathbf{C}}$, while for the coupling matrices defined by Eqs. (14) and (15), $\hat{\mathbf{T}}\hat{\mathbf{N}}_\nu^*\hat{\mathbf{T}}_p = \hat{\mathbf{M}}^+$. This allows rewriting the complex conjugate of Eq. (B3) as

$$\mathbf{b} = -\sum_\nu \hat{\mathbf{C}}\hat{\mathbf{M}}_\nu^+\mathbf{p}_\nu + \hat{\mathbf{C}}\mathbf{a}, \quad \text{(B4)}$$

which upon comparison with Eq. (12) allows identifying important conditions that relate the coupling constants with the direct transmission-reflection matrix:

$$\hat{\mathbf{C}}\hat{\mathbf{M}}_\nu^+ = -\hat{\mathbf{N}}_\nu, \quad \text{(B5)}$$

which is a generalization of similar relations derived previously for an achiral system with a single resonance [25].

The amplitudes (B1) should also obey Eq. (11) with the inversed sign of the time derivative. Multiplying it by $\hat{\mathbf{T}}_p$ and taking the complex conjugate yields

$$-\frac{d\mathbf{p}_\nu}{dt} = q^{(\nu)*}\mathbf{p}_\nu + \hat{\mathbf{T}}_p\hat{\mathbf{M}}_\nu^*\hat{\mathbf{T}}\mathbf{b}. \quad \text{(B6)}$$

Since the coupling matrices (14) and (15) obey also $\hat{\mathbf{T}}_p\hat{\mathbf{M}}_\nu^*\hat{\mathbf{T}} = \hat{\mathbf{N}}_\nu^+$, substituting here $\mathbf{b}$ from Eq. (12) yields

$$\frac{d\mathbf{p}_\nu}{dt} = -q^{(\nu)*}\mathbf{p}_\nu - \sum_{\nu'} \hat{\mathbf{N}}_\nu^+\hat{\mathbf{N}}_{\nu'}\mathbf{p}_{\nu'} - \hat{\mathbf{N}}_\nu^+\hat{\mathbf{C}}\mathbf{a}. \quad \text{(B7)}$$

Using the condition (B5) expressed as $\hat{\mathbf{N}}_\nu^+\hat{\mathbf{C}} = -\hat{\mathbf{M}}_\nu$, one obtains that Eq. (B7) coincides with Eq. (11) provided that

$$\hat{\mathbf{N}}_\nu^+\hat{\mathbf{N}}_{\nu'} = -\delta_{\nu\nu'}[q^{(\nu)} + q^{(\nu)*}] = 2\gamma_r^{(\nu)}\delta_{\nu\nu'}, \quad \text{(B8)}$$

where the radiative damping constant of the $\nu$-th plasmon $\gamma_r^{(\nu)}$ is introduced. In the absence of dissipative losses it provides the only real contribution to $q^{(\nu)}$ and

$$2\gamma_r^{(\nu)} = |m_{\nu+}|^2 + |m'_{\nu+}|^2 = |m_{\nu-}|^2 + |m'_{\nu-}|^2, \quad \text{(B9)}$$

i.e., is naturally determined by the constants of coupling of plasmons to plane waves.

Note also that the condition (B8) imposes a relation on the coupling constants for plasmons with $\nu \neq \nu'$:

$$\left(\frac{m_{1\pm}}{m'_{1\pm}}\right)^* = -\frac{m'_{2\pm}}{m_{2\pm}}. \quad \text{(B10)}$$

This can be seen as a requirement of mutual orthogonality of the complex two-component vectors $(m_{1\pm}, m'_{1\pm})$ and $(m_{2\pm}, m'_{2\pm})$. Therefore, it can be fulfilled only for not more than two plasmon resonances when the matrix $\hat{\mathbf{Q}}_{\nu\nu'}$ is of diagonal form (16). Presumably, models allowing for more than two plasmon resonances should use nondiagonal matrices $\hat{\mathbf{Q}}$.

Altogether, the conditions (B5) and (B8) and the unitarity of the direct transmission-reflection matrix $\hat{\mathbf{C}}$ ensure the reversibility of the system without dissipation losses.

## APPENDIX C: DISSIPATION IN COUPLED-MODE MODEL

Consider the $S$ matrix (17) of the system where the plasmons experience both the dissipative and radiative damping while the other parameters remain unaffected by the dissipation. Then, using the relations (B5) and (B8) one can evaluate

$$\hat{\mathbf{S}}^+\hat{\mathbf{S}} = \left[\hat{\mathbf{C}}^+ - \sum_\nu \frac{\hat{\mathbf{M}}_\nu^+\hat{\mathbf{N}}_\nu^+}{q^{(\nu)*}}\right]\left[\hat{\mathbf{C}} - \sum_\nu \frac{\hat{\mathbf{N}}_\nu\hat{\mathbf{M}}_\nu}{q^{(\nu)}}\right]$$

$$= \hat{\mathbf{I}} + \sum_\nu \left(\frac{1}{q^{(\nu)*}} + \frac{1}{q^{(\nu)}}\right)\hat{\mathbf{M}}_\nu^+\hat{\mathbf{M}}_\nu + \sum_\nu \frac{\hat{\mathbf{M}}_\nu^+\hat{\mathbf{N}}_\nu^+\hat{\mathbf{N}}_\nu\hat{\mathbf{M}}_\nu}{|q^{(\nu)}|^2}$$

$$= \hat{\mathbf{I}} - \sum_\nu \frac{2\gamma^{(\nu)}\hat{\mathbf{M}}_\nu^+\hat{\mathbf{M}}_\nu}{(\omega^{(\nu)} - \omega)^2 + \gamma^{(\nu)2}} + \sum_\nu \frac{2\gamma_r^{(\nu)}\hat{\mathbf{M}}_\nu^+\hat{\mathbf{M}}_\nu}{(\omega^{(\nu)} - \omega)^2 + \gamma^{(\nu)2}}$$

$$= \hat{\mathbf{I}} - \sum_\nu \frac{2\gamma_d^{(\nu)}\hat{\mathbf{M}}_\nu^+\hat{\mathbf{M}}_\nu}{(\omega^{(\nu)} - \omega)^2 + \gamma^{(\nu)2}}, \quad \text{(C1)}$$

where the dissipative damping constants are naturally introduced as the difference between the total and the radiative damping constants: $\gamma_d^{(\nu)} = \gamma^{(\nu)} - \gamma_r^{(\nu)}$. Therefore, the dissipation destroys the unitarity of the $S$ matrix, thus breaking the energy conservation together with the reversibility of the system in general.

According to the $S$-matrix equation (9), the main diagonal of the difference $\hat{\mathbf{I}} - \hat{\mathbf{S}}^+\hat{\mathbf{S}}$ contains the absorption rates for different circular polarizations and sides of incidence, which are then expressed as

$$A_R = 1 - |r|^2 - |t_R|^2 = \sum_\nu \frac{2\gamma_d^{(\nu)}|m_{\nu+}|^2}{(\omega^{(\nu)} - \omega)^2 + \gamma^{(\nu)2}}, \quad \text{(C2)}$$

$$A_L = 1 - |r|^2 - |t_L|^2 = \sum_\nu \frac{2\gamma_d^{(\nu)}|m_{\nu-}|^2}{(\omega^{(\nu)} - \omega)^2 + \gamma^{(\nu)2}}, \quad \text{(C3)}$$

$$A'_R = 1 - |r'|^2 - |t_R|^2 = \sum_\nu \frac{2\gamma_d^{(\nu)}|m'_{\nu-}|^2}{(\omega^{(\nu)} - \omega)^2 + \gamma^{(\nu)2}}, \quad \text{(C4)}$$

$$A'_L = 1 - |r'|^2 - |t_L|^2 = \sum_\nu \frac{2\gamma_d^{(\nu)}|m'_{\nu+}|^2}{(\omega^{(\nu)} - \omega)^2 + \gamma^{(\nu)2}}. \quad \text{(C5)}$$

Being different in magnitude, they exhibit the same Lorentzian frequency dispersion (18) used for the fitting of the numeric data in Sec. III.

The difference of the transmittances of circularly polarized light can be found by taking the difference of Eqs. (C3) and (C2):

$$|t_R|^2 - |t_L|^2 = \sum_\nu 2\gamma_d^{(\nu)} \frac{|m_{\nu-}|^2 - |m_{\nu+}|^2}{(\omega^{(\nu)} - \omega)^2 + \gamma^{(\nu)2}}, \qquad \text{(C6)}$$

which determines CD in Eq. (2). Thus, in terms of the CM model, CD is indeed a direct consequence of the dissipative damping as has been generally shown in Sec. IV A. Note also that the right-hand side in Eq. (C6) tends to zero when one neglects the direct transmission channel by setting $\tau = 0$ and accounts for the relation (B5) for the coupling parameters. This demonstrates explicitly that the Fano-type combination of resonant and background transmissions is critical for the appearance of CD.

Finally, the transmission and reflection amplitudes can be expressed from (17) as

$$t_R = \tau + \sum_\nu \frac{m_{\nu+}m'_{\nu-}}{i(\omega^{(\nu)} - \omega) + \gamma^{(\nu)}}, \qquad \text{(C7)}$$

$$t_L = \tau + \sum_\nu \frac{m'_{\nu+}m_{\nu-}}{i(\omega^{(\nu)} - \omega) + \gamma^{(\nu)}}, \qquad \text{(C8)}$$

$$r = \rho + \sum_\nu \frac{m_{\nu+}m_{\nu-}}{i(\omega^{(\nu)} - \omega) + \gamma^{(\nu)}}, \qquad \text{(C9)}$$

$$r' = \rho' + \sum_\nu \frac{m'_{\nu+}m'_{\nu-}}{i(\omega^{(\nu)} - \omega) + \gamma^{(\nu)}}, \qquad \text{(C10)}$$

and exhibit the frequency dependence (19) typical for the Fano-type transmission resonances.

[1] M. D. Turner, M. Saba, Q. Zhang, B. P. Cumming, G. E. Schröder-Turk, and Min Gu, Nat. Photon. **7**, 801 (2013).

[2] Y. Tang and A. E. Cohen, Phys. Rev. Lett. **104**, 163901 (2010).

[3] Y. Wang, J. Xu, Y. Wang, and H. Chen, Chem. Soc. Rev. **42**, 2930 (2013).

[4] M. Wegener and S. Linden, Physics **2**, 3 (2009).

[5] M. Kuwata-Gonokami, N. Saito, Y. Ino, M. Kauranen, K. Jefimovs, T. Vallius, J. Turunen, and Yu. Svirko, Phys. Rev. Lett. **95**, 227401 (2005).

[6] S. I. Maslovski, D. K. Morits, and S. A. Tretyakov, J. Opt. A: Pure Appl. Opt. **11**, 074004 (2009).

[7] K. Dietrich, C. Menzel, D. Lehr, O. Puffky, U. Hübner, T. Pertsch, A. Tünnermann, and E.-B. Kley, Appl. Phys. Lett. **104**, 193107 (2014).

[8] M. Decker, R. Zhao, C. M. Soukoulis, S. Linden, and M. Wegener, Opt. Lett. **35**, 1593 (2010).

[9] Y. Zhao, M. A. Belkin, and A. Alu, Nat. Commun. **3**, 870 (2012).

[10] J. H. Singh, G. Nair, A. Ghosh, and A. Ghosh, Nanoscale **5**, 7224 (2013).

[11] J. G. Gibbs, A. G. Mark, S. Eslami, and P. Fischer, Appl. Phys. Lett. **103**, 213101 (2013).

[12] M. V. Gorkunov, A. A. Ezhov, V. V. Artemov, O. Y. Rogov, and S. G. Yudin, Appl. Phys. Lett. **104**, 221102 (2014).

[13] M. V. Gorkunov, V. E. Dmitrienko, A. A. Ezhov, V. V. Artemov, and O. Y. Rogov, Sci. Rep. **5**, 9273 (2015).

[14] W. L. Barnes, J. Opt. A: Pure Appl. Opt. **11**, 114002 (2009).

[15] K. L. Kelly, E. Coronado, L. L. Zhao, and G. C. Schatz, J. Phys. Chem. B **107**, 668 (2003).

[16] M. V. Gorkunov, B. I. Sturman, and E. V. Podivilov, Europhys. Lett. **110**, 57004 (2015).

[17] E. V. Podivilov, B. I. Sturman, and M. V. Gorkunov, J. Opt. Soc. Am. B **29**, 3248 (2012).

[18] R. Kolkowski, L. Petti, M. Rippa, C. Lafargue, and J. Zyss, ACS Photon. **2**, 899 (2015).

[19] A. C. Lesina, A. Vaccari, P. Berini, and L. Ramunno, Opt. Express **23**, 010481 (2015).

[20] S. V. Jayanti, J. H. Park, A. Dejneka, D. Chvostova, K. M. McPeak, X. Chen, S.-H. Oh, and D. J. Norris, Opt. Mater. Express **5**, 1147 (2015).

[21] V. P. Drachev, U. K. Chettiar, A. V. Kildishev, H.-K. Yuan, W. Cai, and V. M. Shalaev, Opt. Express **16**, 1186 (2008).

[22] Schmid & Partner Engineering AG, SEMCAD X Reference Manual, 118, November 2013.

[23] D. W. Lynch and W. R. Hunter, in *Handbook of Optical Constants of Solids*, edited by E. D. Palik (Academic, New York, 1985).

[24] H. A. Haus, *Waves and Fields in Optoelectronics* (Prentice-Hall, Englewood Cliffs, NJ, 1984).

[25] S. Fan, W. Suh, and J. D. Joannopoulos, J. Opt. Soc. Am. A **20**, 569 (2003).

[26] J. W. Yoon, M. J. Jung, S. H. Song, and R. Magnusson, IEEE J. Quantum Electron. **48**, 852 (2012).

[27] V. V. Klimov, I. V. Zabkov, A. A. Pavlov, R.-C. Shiu, H.-C. Chan, and G. Y. Guo, Opt. Express **24**, 6172 (2016).

[28] J. Kaschke, J. K. Gansel, and M. Wegener, Opt. Express **20**, 26012 (2012).

[29] C. Menzel, C. Rockstuhl, and F. Lederer, Phys. Rev. A **82**, 053811 (2010).

[30] B. Hopkins, A. N. Poddubny, A. E. Miroshnichenko, and Yu. S. Kivshar, Laser Photon. Rev. **10**, 137 (2016).

[31] K. Hannam, D. A. Powell, I. V. Shadrivov, and Y. S. Kivshar, Phys. Rev. B **89**, 125105 (2014).